

Compression fatigue of elastomeric foams used in midsoles of running shoes

C. Aimar^{a,b}, L. Orgéas^{a*}, S. Rolland du Roscoat^a, L. Bailly^a, D. Ferré Sentis^b

^aUniv. Grenoble Alpes, CNRS, Grenoble INP[†], 3SR Lab, 38000 Grenoble, France;

^bDecathlon SA, Footwear International Division, Lille, France

*Corresponding author: laurent.orgeas@3sr-grenoble.fr

[†]Institute of Engineering Univ. Grenoble Alpes

Compression fatigue of elastomeric foams used in midsoles of running shoes

Due to their excellent specific mechanical properties, closed cell elastomeric foams are the main element in the soles of running shoes to absorb repetitive shocks from strides and to release a maximum of the absorbed energy. However, these cellular materials are gradually damaged. To enhance their mechanical durability by slowing their damage kinetics, it is critical to understand their mechanical behaviour in fatigue. The objective of this work is thus to clarify the link between the microstructure and the fatigue properties of five commercial elastomeric foams used in the midsoles of running shoes. The 3D cellular structures of each foam were finely analysed using X-ray microtomography. Foam samples were then subjected to cyclic compression which were close to running conditions. During cycling, samples exhibited a rapid densification associated with noticeable decreases of the stress levels required to deform them as well as the cushioning and the rebound properties. We show that the two midsoles filled with micro-sized mineral fillers present the highest specific mechanical properties during the first compression cycle and during fatigue. However, their damage kinetics and rebound properties could probably be improved by tuning the fillers-matrix compatibility. The lighter foam, being very porous and presenting process-induced tortuous cell walls, is the best cushioning system but exhibits high damage kinetics. The denser foam presents poor specific mechanical properties, but a very slow damage kinetics. Its double hierarchical architecture probably prevents the occurrence of micro-cracks in the cell walls.

Keywords: Midsoles – Elastomeric foams – Compression fatigue – X-ray microtomography - Microstructure

1 **Introduction**

2 The optimal stride frequency (Cavanagh et Kram 1989) of an elite long distance runner
3 is around 4800 strides per hour (Musgjerd et al., 2021; Oeveren et al., 2017). During
4 strides, the foot-ground reaction forces exhibit repeated compressive loadings (Nigg et
5 al., 2012). Fig.1a shows the heel landing (first peak) and the forefoot propulsion (second
6 peak) during the first 200 ms for a 75 kg man running at 12 km h⁻¹ (Clarke et al., 1983).
7 In this example, the duration of the aerial phase is 600 ms, before the next stride. The
8 double peak characteristics typically depend on the technique of the athlete, his/her
9 morphology and speed. Thus, the shoe lifetime depends on the use and the user as well
10 as the grade of the material, and is more or less around 500 km (Rethnam & Makwana,
11 2011). The current market trend is to extend this lifetime.

12 To limit mechanical efforts sustained by the body, improve running comfort and
13 avoid injuries (Malisoux et al., 2019; Taunton et al., 2002, 2003) athletes use dedicated
14 running shoes, fitted with a multilayered sole (Fig. 1b and c). The outsole is the layer in
15 contact with the floor, the insole is in contact with the foot, and the midsole is in between.
16 The midsole is the main energy absorbing-releasing system of standard soles (Sun et al.,
17 2020). On the one hand, it must be lightweight to minimize the energy expended by the
18 runner (Franz et al., 2012; Fuller et al., 2015; Hoogkamer et al., 2016). On the other hand,
19 it must be as energy absorbent as possible during the stride ground phase, while releasing
20 in the same time a maximum of energy for an efficient propulsion of the feet in the air
21 (Frederick et al., 1986; Sinclair et al., 2016; Worobets et al., 2014).

22 Usually, such specifications are achieved by tuning, the geometry of the midsole
23 (*e.g.*, its thickness (Chambon et al., 2014) and/or the difference in height between rear-
24 foot and forefoot areas (Chambon et al., 2013)), and/or the choice of constitutive materials

(Malisoux et al., 2019; Silva et al., 2009), for instance by combining cellular materials (Brückner et al., 2010) to optional hard inserts (*e.g.*, gel, stiff plates as in Fig.1b-A (Flores et al., 2019; Madden et al., 2016)) and/or air volume as in Fig.1b-B.

To date, solid elastomeric foams with closed cells remain the preferred candidates for midsoles (Fig.1b and c) (Brückner et al., 2010; Mills, 2007; Verdejo & Mills, 2002) due to their relevant specific mechanical properties (Shimazaki et al., 2016), their low-cost and to their versatile and fast manufacturing processes. In particular, ethylene-vinyl-acetate (EVA) based foams are the most widely used for the last four decades (Mills, 2007; Sun et al., 2020). Recently, thermoplastic polyurethane (TPU) and polyether-block-amide (PEBA) based foams were also praised by the running community (Brückner et al., 2010; Chen et al., 2022). These cellular systems exhibit a typical compressible visco-hyperelastic behaviour with good energy absorption-release properties (L. J. Gibson & Ashby, 1999). Over a high number of load-unload cycles during training, the evolution of mechanical properties of midsole foams results in a progressive densification associated with a loss of cushioning properties (Cornwall & McPoil, 2017).

Among the challenges to overcome to restrain the damage kinetics of closed cell elastomeric foams, identifying and understanding their fatigue mechanisms and their links with their structural properties is a critical issue. To this end, two main experimental approaches are found in the literature. One is a field-based approach studying midsoles used during real training sessions (Malisoux et al., 2019; Verdejo & Mills, 2004a). More particularly, Verdejo *et al.* collected EVA midsoles samples from the sole of a used running shoe and characterized their microstructures using scanning electron microscopy. The 2D micrographs showed holes in cell walls under the heel pad area and buckled cell walls in the forefoot area, giving a first microstructural insight on the fatigue of EVA

midsoles (Verdejo & Mills, 2004a). However, the high number of interfering parameters (*e.g.*, humidity, temperature (Kinoshita & Bates, 1996) ground types (Taylor et al. 2012) morphologies and techniques of runners (Malisoux et al., 2019)), and the time required to conduct such experiments remain major obstacles to this approach.

To circumvent these difficulties, a second approach consists in studying midsoles compressed in laboratory by subjecting foam samples to mechanical loadings close to those undergone during running. These studies highlighted that aging mechanisms due to gas loss by diffusion through the closed cell walls were negligible in fatigue (Verdejo & Mills, 2004b) and that chemical modifications observed by Fourier-transform infrared spectroscopy of the solid phase were observed after fatigue, but the reaction is not yet identified (Lippa et al., 2014). These studies also provided guidelines to better understand aging mechanisms of the midsoles. However, they were restricted to EVA foams, leaving aside the new material formulations proposed on the market. In parallel, in the past decade, X-ray microtomography (μ CT in the following) has become a reference 3D imaging technique to characterize the microstructure of cellular materials with micro to millimetric pore sizes (Pardo-Alonso et al., 2015; Patterson et al., 2016) and more recently to characterize midsole cellular microstructures (Singaravelu et al., 2020). However, up to date, no information has been provided about the 3D microstructures of midsole foams together with their effect on the mechanical behaviour of such materials.

Therefore, the objective of this work is to better understand the fatigue of commercial elastomeric foams used in the midsoles of running shoes by clarifying the relationship between their process-induced 3D microstructures, which were characterized with μ CT, and their behaviour during cyclic compression. The results provide guidelines to enhance midsole foams performances.

Materials and methods

Shoes and midsoles foam samples

Experiments were conducted by using midsoles from four top-of-the-range commercial running shoes (Fig.1b and c, obtained by μ CT at low spatial resolution, *cf.* next subsection). Qualitative mechanical and structural performances of midsoles claimed by the manufacturers are detailed in Tab.1. The cushioning of midsoles represents their energy absorption capability, while the rebound represents their capability to release the energy stored during compression with a minimum of dissipation, *i.e.*, with minimum viscous or plastic damping. The durability of the foams refers to the conservation of the mechanical properties during the shoe lifetime and thus, to a slow damage kinetics. In addition, midsoles must be as light as possible in order to minimize the energy expended by the runner during training. For this reason, the specific mechanical properties of foams, as defined by Gibson and Ashby (L. J. Gibson & Ashby, 1999), are also relevant performance indicators for midsoles. Foam samples, F_1 , were extracted from the midsoles of the four running shoes (Fig. 1b and c). Samples F_2 and F_2^* respectively derived from the main material and from the insert of the second studied midsole (Fig. 2c-2). The selected midsole foams differed by the nature of their parent polymer, *i.e.*, EVA, TPU, PEBA.

After separating the upper part from the sole using a bandsaw machine, a slitting machine was used to obtain slices of height $h_0 = 2$ mm of the midsoles to characterize both the structure and the fatigue of the midsoles. Due to industrial processes, midsoles present local density variation at the sample scale (Fig. 1b and c). For this reason, the density of three larger samples (in-plane dimensions: 20 mm long, 20 mm wide) was measured for each midsole to obtain an averaged density ρ , estimated using a calliper

(precision: 0.01 mm) and a microbalance (precision: 0.1 mg). We extracted from these sheets smaller samples for mechanical testing, the density of which equal to the corresponding averaged value of each midsole $\pm 0.01 \text{ g cm}^{-3}$. Thus, we used cylindrical samples (Fig. 2A, in-plane diameter $d_0 = 2 \text{ mm}$) for foams F_1 , F_2 and F_4 . For the TPU foam F_3 , made of welded expanded pellets (Fig. 1c-3), larger cuboid samples were cut using a razor blade (in-plane square area: $10 \times 10 \text{ mm}^2$) to allow representative mechanical characterization of the midsole. Samples were maintained at 55 % RH and $T=22 \text{ }^\circ\text{C}$ from their extraction to the end of all experiments.

Structure characterization

At macroscale, we used a laboratory X-ray tomograph manufactured by RX Solutions to visualize the vertical slices of soles shown in Fig. 1b (parameters are given in appendix). At microscale, the 3D microstructure of each sample was analysed using the same tomograph equipped with another X-ray source. Samples were placed on a long thin alumina rod (2 mm diameter, 10 cm length) close to the X-ray source to obtain a voxel size of $1 \text{ }\mu\text{m}^3$. The parameters were: source type: Hamamatsu equipped with a lanthanum hexaboride filament, mode: middle spot, detector flat panel: VARIAN, tension: 60 kV, target current: $7 \text{ }\mu\text{A}$, frame rate: 1 s^{-1} , number of averaged frames: 3, number of projections: 2400. The reconstruction was done using X-Act software based on a filtered backprojection algorithm. Images were segmented using the plugin 3D weka segmentation (Arganda-Carreras et al., 2017) available on Fiji (Schindelin et al., 2012) (see example in Fig. 1b). Various image analysis procedures were applied to the segmented volumes to quantify the 3D microstructure descriptors of each sample. The porosity ϕ , the mean pore size $C \text{ (}\mu\text{m)}$ and the mean cell wall thickness $t \text{ (}\mu\text{m)}$ were

estimated using the function *Thickness* of the plugin BoneJ (Doubé et al., 2010) for the two latter mentioned structural parameters (see detailed procedure in appendix).

Cyclic compression tests

Foam samples were subjected to simple compression fatigue tests using a standard electromechanical device (Instron 05944 equipped with a ± 10 N loadcell maximal capacity). Samples were placed between 2 parallel compression platens (30 mm x 30 mm), coated with a very thin layer of silicon oil (compared to the sample size) acting as a lubricant to avoid any sample barreling effect induced by friction forces between the sample and the platens (Chalencon et al., 2010, Guiraud et al., 2012). During the tests, the axial compression force f_z was recorded to calculate the nominal compression stress $\sigma = |4f_z / (\pi d_0^2)|$ and the displacement of the crosshead δ was measured in order to calculate the compression natural strain $\varepsilon = |\ln(h/h_0)|$ (also known as the Hencky strain), where $h = h_0 + \delta$ is the actual sample height.

The design of the testing procedure was achieved by accounting for three constraints, *i.e.*, with the objective to constitute a database that could be useful both for (i) running shoe design and (ii) fundamental knowledge in materials science and that could be (iii) achieved with our experimental facilities. Bearing in mind this framework, we performed cyclic compression tests using a strain-controlled approach, in accordance with the literature dedicated to the fatigue of elastomers under finite strains (Le Saux et al., 2010, Lo et al., 2015). Hence, each cycle consisted in subjecting the samples to a representative compression up to a maximal strain $\varepsilon^{max} = 1.6$ and to unload it down to a minimal strain $\varepsilon^{min} = 0$. The chosen value of the maximal strain corresponds to a typical strain undergone by the midsole under the heel bone during the heel impact phase of a rearfoot

strike pattern stride (Verdejo & Mills 2002, Verdejo 2004). In addition, for each compression cycle, tests were performed at the compression strain rate $|\dot{\delta}/h_0| = 4 \text{ s}^{-1}$, during loading and during unloading. It was the highest strain rate we could properly achieve with the Instron device. The resulting cycling frequency was 1.25 Hz, being slightly lower than the commonly admitted running stride frequencies (1.3 to 1.6 Hz, (Atwater 1990; Cavanagh et Kram 1989; Verdejo & Mills, 2002; Verdejo 2004)). However, possible strain rate effects on the viscoelastic properties which would be induced by this difference of only $\approx 15\%$ are supposed to be negligible accounting for the polymers under consideration (Aurilia et al. 2011; Carotenuto et al. 2019; Diani 2020). In addition, it must be pointed out that during the unloading phase of each cycle, the compression force systematically reaches the zero value before the zero value of the minimal cycling strain ε^{min} . Hence, during this period, samples are subjected to a partial free stress recovery, which roughly resembles the partial free stress recovery experienced by the midsole when the shoe is not touching the ground. At last, to study fatigue-induced effects, each compression cycle was repeated to reach a total number of cycles $N = 200000$, leading to a test duration of approximately 45 h. Using typical running frequencies and velocities measured in the literature, respectively ranging between 1.3 and 1.6 Hz and between 10 and 20 km h⁻¹ (Atwater 1990; Cavanagh et Kram 1989; Verdejo & Mills, 2002; Verdejo 2004), the considered tests should thus roughly correspond to running distances ranging between 400 and 700 km.

To check the repeatability, fatigue tests were conducted on three different samples for each foam. Considering the small stress variations between samples, being lower than $\pm 5\%$, and for the sake of clarity, only one mechanical response per tested foam is reported in the following. A typical response (sample F₁) to a first load-unload compression cycle is illustrated in Fig. 2. During loading, the compression behaviour is usually divided into

three densification steps delimited by ε_c and by ε_d : (i) a sharp increase of the stress level corresponding to the quasi-linear deformation of cell walls up to a compression yield strengths σ_c , followed by (ii) a slow increase of the stress level during which cell wall buckling is considered to occur, followed by (iii) a sharp increase of the stress level when the porosity is low enough for cell walls to enter in contact with one another (L. J. Gibson & Ashby, 1999). Five other properties were extracted for each cycle and monitored in fatigue:

- The cushioning properties was gauged as the volumetric absorbed energy during loadings: $W_{abs}(\sigma) = \int_{\varepsilon^0}^{\varepsilon} \sigma(\varepsilon') d\varepsilon'$, where ε^0 is the strain of the sample at the beginning of each loading (*e.g.*, Fig. 1A for $N = 1$)
- Two specific mechanical properties evaluated at the end of loadings (at ε^{max} , Fig. 2M) to compare the foams performances, taking into account their weight (I. J. Gibson & Ashby, 1982):
 - The maximum specific stress, *i.e.*, the stress normalized by the density of foams σ^{max} / ρ .
 - The associated maximum specific absorbed volumetric energy W_{abs}^{max} / ρ , where W_{abs}^{max} is the area under the loading curve.
- The damping loss factor η was also extracted to gauge the rebound properties at the end of unloadings: $\eta = W_{diss}^{max} / (\pi W_{abs}^{max})$ (Gadot, 2015; Zhang et al., 2013), where W_{diss}^{max} is the area of the hysteresis cycle (Fig. 2). The lower the damping loss factor, the better the release of the stored energy.

- The residual strain ε^{res} was estimated at the end of loadings in order to evaluate the foam recovery between cycles and their progressive densification upon cycling (Fig. 2R).

Results

Structural characterization

Density

The foam densities, ρ , are reported in Tab. 2. These values lie between 0.09 g cm^{-3} for the PEBA foam F₄ and 0.24 g cm^{-3} for the TPU foam F₃, in agreement with the average values reported for athletic shoe midsoles $\approx 0.2 \text{ g cm}^{-3}$ (Brückner et al., 2010; Mills, 2007; Verdejo & Mills, 2004a).

Microstructure

The slices reported in Fig. 3 shows the inner microstructures of each foam along the compression direction. The corresponding quantitative descriptors are given in Tab. 2. The results bring up the following comments:

- All microstructures exhibit mainly closed cells at the observation scale: due to the chosen spatial resolution used to image samples, some very thin cell walls ($< 2 \mu\text{m}$) as well as holes in these walls are not easily detected and some cells may be connected.
- Micro-sized mineral fillers, which absorb more X-ray than the polymer matrix, are observed in EVA foams F₁, F₂ and F₂^{*}. They are poorly dispersed with an average size ranging from $7 \mu\text{m}$ to $2 \mu\text{m}$.
- The EVA foam F₂^{*} presents a lower porosity of 0.71 and a higher density of 0.23 g cm^{-3} than the EVA foam F₁ (exhibiting a porosity of 0.79 and a

density of 0.17 g cm^{-3}). The average wall thickness distribution of F_2^* presents a normalized standard deviation of 61 % which is larger than that estimated for F_1 (44 %). Thus, F_2^* exhibits a more heterogeneous microstructure than F_1 .

- The TPU foam F_3 presents the second lowest porosity of 0.72, in agreement with its density of 0.24 g cm^{-3} . It exhibits small pores and thin cell walls close to the edges of expanded pellets and larger ones close to their cores. Such microstructure size gradient is similar to the one observed by Singaravelu *et al.* (Singaravelu et al., 2020), making echo to fruit peel microstructure used as natural cushioning system (Li et al., 2019). Due to the presence of a skin at the surface of each pellet, F_3 microstructure is hierarchically architected.

- The PEBA foam F_4 displays by far the most porous microstructure with a porosity of 0.90, and the most tortuous cell walls.

Mechanical characterization

The stress-strain responses during the first cycle ($N = 1$) are presented in Fig. 4a for each tested foam. The associated mechanical properties are reported in Tab. 2. Similarly, the stress-strain responses during the last cycle ($N = 200000$) are presented in Fig. 4b for each foam. Fig. 4c and d show the volumetric absorbed energy diagram at $N = 1$ and at $N = 200000$ to assess the foam performance in absorbing a maximum of energy for a minimal stress, as suggested by Gibson and Ashby (L. J. Gibson & Ashby, 1999). In order to clarify the link between the foam microstructures and their energy absorption capabilities (L. J. Gibson & Ashby, 1999), we have reported in the graphs d, e and f of Fig. 4 (at $N = 1$ and $N = 200000$, respectively) the evolution of the volumetric absorbed

energy diagram normalized by the Young modulus of the parent polymer E_{P_i} ($E_{EVA} = 18$ MPa, $E_{TPU} = 10$ MPa, $E_{PEBA} = 20$ MPa (Arkema; BASF; Verdejo & Mills, 2002). In addition, to evaluate the performance of foams relative to their weight and their damage kinetics upon cycling, the evolutions of the specific mechanical properties σ^{max} / ρ and W_{abs}^{max} / ρ with the number of cycles N have been reported in Fig. 5a and b, respectively. Lastly, to gauge the rebound and the recovery properties of foams during fatigue as well as their damage kinetics, the evolution of the damping loss factor η and ε^{res} are presented in Fig. 5c and d, respectively.

First cycle

During the first loadings shown in Fig. 4a, all foams exhibit the first densification phase (i) except the PEBA foam F4. The second and third densification phases, (ii) and (iii), are observed for all foams, resulting in a behaviour typically observed for closed cell elastomeric foams (L. J. Gibson & Ashby, 1999). During unloading, the area of hysteresis cycle, between 0.29 MJ m^{-3} and 0.07 MJ m^{-3} for all foams, is typical of such materials used in midsoles (Verdejo & Mills, 2004b): the first points reported in Fig. 5c prove that foams F3 and F4 initially exhibit the lowest damping loss factor. It is interesting to note from Fig. 4c that (i) below a threshold stress of $\approx 0.2 \text{ MPa}$, *i.e.*, in the early stage of the stride, the foam F4 absorbs more energy (and thus should bring better shock attenuation) than F3, which in turn absorbs more energy than the other tested foams, (ii) this trend is annealed above this threshold. Also, results of Fig. 4e prove that the aforementioned trends should be ascribed to the foam morphology for foam F4, and to the high density and/or the hierarchical architecture for foam F3. Lastly, regarding the initial specific properties, the first points of Fig. 5a and b show that F1, F2 (and in a less extend F4) exhibit

the best specific stresses and absorbed energies. These features constitute interesting properties for lightweight design of midsoles.

Effect of cycling

In Fig. 4b, the hysteresis cycles at $N = 200000$ are thinner than in Fig. 4a at $N = 1$, and exhibit an offset to higher strain values than in Fig. 4a at $N = 1$. In Fig. 5a to d, the evolutions of the four mechanical properties illustrate the damage kinetics upon cycling of all foams. The mean overall evolutions are: $-42 \pm 6 \%$ for the maximum specific stress (Fig. 5a), $-66 \pm 15 \%$ for the maximum specific volumetric absorbed energy (Fig. 5b), $-26 \pm 3 \%$ for the damping loss factor (Fig. 5c) and $+340 \pm 107 \%$ for the residual strain (Fig. 5d). In addition, the decrease of the maximum specific stress upon cycling illustrates the softening of the foams. It was observed in previous work on polymeric foams during the first hundreds compression cycles (Shen et al., 2001). It echoes the Mullin's effect observed for dense elastomers (Mullins, 1969). This result is correlated with the decrease in the maximum specific volumetric absorbed energy. Furthermore, the overall damping loss factor evolutions are correlated with the densification of the foams during cycling, *i.e.*, the progressive increases of ε^{res} . The increase in the damping loss factor between cycles $N = 100$ and 4000 , observed for the three EVA foams and the PEBA foam, illustrates that the dissipated energy decreases faster than the absorbed one. Furthermore, during the last loading (Fig. 4b), no foam exhibits the first densification phase (i). In agreement with our previous observation on the process-induced microstructure of the PEBA foam F₄ at $N = 1$, the fatigue-induced microstructures of all foams are suspected to exhibit tortuous cell walls which could be progressively induced during cycling. Also, the trends reported in the previous section for the absorbed energies (Fig. 4c) more or less vanish after cycling (Fig. 4d), this being probably due to a detrimental cycling induced-

microstructure evolution. At last, the decreases of the specific stresses (Fig. 5a) and absorbed energies (Fig. 5b) for the three “best” (from the specific standpoint, *i.e.*, when an optimal lightweight design is sought) initial foams upon cycling are faster than those reported for the two other foams.

Discussion

Effect of the microstructure features on the stress-strain behaviour

It is worth noticing that the process-induced tortuous/buckled cell walls of the PEBA foam F₄ (Fig. 3) should probably explain why F₄ does not exhibit the first densification phase (i). In addition, Fig. 4a proves that the EVA foams F₁, F₂ and F₂^{*} reach higher compression stress σ^{max} than the TPU foam F₃ which is the denser studied foam (Tab. 2). Also, in Fig. 5a and b at $N = 1$, the two specific mechanical properties of the EVA foams are higher than for the TPU foam F₃. The possible reason for that is the use of micro-fillers in the EVA foams, acting as reinforcements to enhance the foam specific mechanical properties. However, as shown in Fig. 4a and as quantified in Fig. 5c and d for $N = 1$, such reinforced materials present wider hysteresis cycles, larger damping loss factor η and larger residual strain ε^{res} than the TPU and the PEBA foams F₃ and F₄. In the literature, filled dense rubbers are known to exhibit higher dissipation energy than unfilled ones (Mzabi et al., 2011). A possible explanation to this behaviour is a low compatibility of micro-mineral fillers with the elastomeric EVA matrix. A more cohesive interface between the fillers and the polymer matrix would probably reduce the dissipated energy (*i.e.*, decreases the value of η) of such reinforced midsoles. Furthermore, in the case of filled EVA foams, F₁ presents higher specific mechanical properties than F₂^{*}, despite its higher porosity (Fig. 5a and b at $N = 1$). We believe that the heterogeneity in cell size and wall thickness of F₂^{*} (Tab. 2) should contribute to lower its specific

mechanical properties. An optimized microstructure, possibly tailored by the type and the amount of blowing agent used, would certainly improve the performance of F_2^* .

Energy absorption diagram and optimal microstructures

In Fig. 4c, all foams present an abrupt change in their absorbing behaviour above their compression yield strengths σ_c (Tab. 2), which is typical of closed cell elastomeric foams (L. J. Gibson & Ashby, 1999). The optimal behaviour of a cushioning system tends to maximize the energy absorbed while minimizing compression stress (L. J. Gibson & Ashby, 1999). For $\sigma < 0.2$ MPa, corresponding to the very beginning of the stride, the PEBA foam F_4 is, by far, the best energy absorption system. Then comes the TPU foam F_3 , followed by all EVA foams, F_1 , F_2 and F_2^* . For $\sigma > 0.2$ MPa, all foams follow a master curve. Fig. 4e shows the energy diagram of all foams normalized by the Young modulus of each solid phase, to assess the microstructure cushioning efficiency (L. J. Gibson & Ashby, 1999). This graph proves that the PEBA foam F_4 shows the best microstructure energy absorption system whatever the applied stress. The process-induced tortuous cell walls of F_4 microstructure, associated with a highly porous and homogeneous structure probably enhances the maximisation of the energy absorption while minimising the compression stress. This is in agreement with the literature according to which buckling of the walls is the main energy absorption mechanism (L. J. Gibson & Ashby, 1999). The EVA foams F_1 , F_2 and F_2^* are the second best microstructures for an efficient energy absorption system. However, the three EVA foams remain difficult to distinguish from each other because they display a porosity ranging from 0.79 to 0.71, a density ranging from 0.13 to 0.23 g cm⁻³, a microstructure homogeneity ranging from 23 to 61 % and a more or less tortuous microstructure. The TPU foam F_3 microstructure is the least efficient. With a closer look to the EVA foams F_2^* and the TPU foam F_3 , which present

the same density, we conclude that the highly heterogeneous hierarchical architected microstructure of F₃ is not so relevant compared to the less heterogeneous microstructure of F₂^{*}.

Effect of cycling

In Fig. 5a and b, the EVA foams F₁ and F₂, with micro-sized fillers and displaying a homogeneous microstructure, belong to the set of foams with the highest specific mechanical properties upon cycling. Thus, the added value of the reinforcing micro-sized fillers is still visible on the specific properties of foams in fatigue. However, in Fig. 5a to d, they lose 35 to 40 % of their initial σ^{max}/ρ , 70 % of their initial W_{abs}^{max}/ρ , 73 to 80 % of their initial η and gain 304 to 307 % of their initial ε^{res} upon cycling. Thus, their damage kinetics are faster than those reported for the foam F₃. Besides, they still exhibit higher damping loss factor η than the PEBA and the TPU foams F₄ and F₃ (Fig. 5c). Micro-sized fillers may damage the walls upon cycling, increasing their rebound properties and speed up the damage kinetics by creating fillers/matrix decohesion as in filled rubber during fatigue (Le Cam et al., 2008).

In Fig. 5a to d, one note that the TPU foam F₃ loses 25 % of its initial σ^{max}/ρ , 40 % of its initial W_{abs}^{max}/ρ , 66 % of its initial η , and gains only 200 % of its initial ε^{res} upon cycling. Despite its much lower specific mechanical properties, F₃ exhibits the slowest damaged kinetics of all other foams by better maintaining its mechanical properties. For these reasons, it can be considered a relevant target as a mechanically durable midsole. Both, the high density of the TPU foam F₃ and its double hierarchical architecture probably play a major role in the durability of the foam. The skin envelope of each expanded pellet (Fig. 3) could restrain micro-failure cracks initiation and propagation.

Conclusion

Elastomeric foams used as systems for absorbing-releasing energy in the midsoles of running shoes are complex architected cellular materials. Their mechanical properties depend on (a) their densities, (b) their microstructures features including micro-fillers, pore/cell wall size and shape, and (c) the polymer constituting their solid phases (here: EVA, TPU and PEBA). The whole of these structural features are closely linked to their manufacturing processes.

The foam microstructure plays a major role on mechanical properties during the first compression cycle but also upon cycling. The foam that presents the highest porosity associated with the most tortuous cell walls and with a very homogeneous microstructure is the best cushioning system during the first cycles. However, its damage kinetics upon cycling is rather fast. Micro-sized fillers in the EVA foams act as reinforcements to enhance the foam specific mechanical properties, but due to the probable weak cohesion of the fillers with the polymer, the foam rebound properties are hindered by important dissipated energy, and their damage kinetics is enhanced. Thus, a proper functionalization of the fillers would probably improve the matrix-fillers cohesion and thus mechanical properties and durability of the reinforced foams. With poor initial specific mechanical properties, the foam exhibiting the slowest damage kinetics displays a dense and hierarchical architected microstructure that should prevent micro-cracks initiation and propagation. Hence, the trade-off between an optimal energy absorbing/releasing cellular microstructure combined with both a slow damage kinetics and the lightweight design constraint remains a great challenge for midsole manufacturers. Further studies on the

390 evolution of the microstructure during fatigue, and, in parallel, on the development of
391 more biofidelic fatigue tests should confirm/complete these remarks and should provide
392 stronger guidelines to enhance the midsoles design and properties.

Acknowledgements

This work was supported by the ANRT under Grant 2019/1038 and Decathlon. 3SR is part of LabEx Tec 21 - ANR-11-LABX-0030 and of Institut Carnot PolyNat (ANR16-CARN-0025).

Declaration of interest statement

The authors report there are no competing interests to declare.

References

- Arganda-Carreras, I., Kaynig, V., Rueden, C., Eliceiri, K. W., Schindelin, J., Cardona, A., & Sebastian Seung, H. (2017). Trainable Weka Segmentation: A machine learning tool for microscopy pixel classification. *Bioinformatics*, 33(15), 2424–2426. <https://doi.org/10.1093/bioinformatics/btx180>
- Arkema. (n.d.). *Peebax*. Retrieved 26 October 2022, from <https://hpp.arkema.com/en/product/-families/pebax/-elastomer/-family/>
- Atwater, Anne. 1990. Gender Differences in Distance Running. In *Biomechanics of Distance Running*, Human Kinetics, Champagne, IL , 321-62.
- Aurilia, Marco, Filomena Piscitelli, Luigi Sorrentino, Marino Lavorgna, et Salvatore Iannace. 2011. Detailed analysis of dynamic mechanical properties of TPU nanocomposite: The role of the interfaces. *European Polymer Journal* 47 (5): 925-36. <https://doi.org/10.1016/j.eurpolymj.2011.01.005>.
- BASF. (n.d.). *Elastollan® (TPU)—The thermoplastic polyurethane of BASF*. Retrieved 26 October 2022, from https://plastics-rubber.basf.com/global/en/performance_polymers/products/elastollan.html

- Benedetti, M., du Plessis, A., Ritchie, R. O., Dallago, M., Razavi, S. M. J., & Berto, F. (2021). Architected cellular materials: A review on their mechanical properties towards fatigue-tolerant design and fabrication. *Materials Science and Engineering: R: Reports*, 144. <https://doi.org/10.1016/j.mser.2021.100606>
- Brückner, K., Odenwald, S., Schwanitz, S., Heidenfelder, J., & Milani, T. (2010). Polyurethane-foam midsoles in running shoes—Impact energy and damping. *Procedia Engineering*, 2(2), 2789–2793. <https://doi.org/10.1016/j.proeng.2010.04.067>
- Carotenuto, C., Liana P. P., Luigi G., et Mario M. 2019. Viscoelasticity Evolution of Ethylene-Vinyl-Acetate Copolymers During Crystallization. *Chemical Engineering Transactions* 74 (mai): 1093-98. <https://doi.org/10.3303/CET1974183>.
- Cavanagh, P.R., Kram R. (1989). Stride length in distance running: velocity, body dimensions, and added mass effects. *Medicine and Science in Sports and Exercise* 21 (4): 467-79.
- Chalencon, F., Dumont, P.J.J., Orgéas, L., Foray, G., Cavaillé, J.-Y., Maire, E., Rolland du Roscoat. (2010). Lubricated compression and X-ray microtomography to analyse the rheology of a fibre-reinforced mortar. *Rheologica Acta* 49 p. 221-235 <https://doi.org/10.1007/s00397-009-0393-5>
- Chambon, N., Delattre, N., Berton, E., Gueguen, N., & Rao, G. (2013). The effect of shoe drop on running pattern. *Footwear Science*, 5(sup1), S106–S107. <https://doi.org/10.1080/19424280.2013.799585>
- Chambon, N., Delattre, N., Guéguen, N., Berton, E., & Rao, G. (2014). Is midsole thickness a key parameter for the running pattern? *Gait and Posture*, 40(1), 58–63. <https://doi.org/10.1016/j.gaitpost.2014.02.005>

- Chen, S.-C., Lee, K.-H., Chang, C.-W., Hsu, T.-J., & Feng, C.-T. (2022). Using Gas Counter Pressure and Combined Technologies for Microcellular Injection Molding of Thermoplastic Polyurethane to Achieve High Foaming Qualities and Weight Reduction. *Polymers*, 14(10), 2017.
<https://doi.org/10.3390/polym14102017>
- Clarke, T. E., Frederick, E. C., & Cooper, L. B. (1983). Effects of shoe cushioning upon ground reaction forces in running. *International Journal of Sports Medicine*, 4(4), 247–251. <https://doi.org/10.1055/s-2008-1026043>
- Cornwall, M. W., & McPoil, T. G. (2017). Can runners perceive changes in heel cushioning as the shoe ages with increase mileage ? *International Journal of Sports Physical Therapy*, 12(4), 616–624.
- Diani, J. 2020. Free vibrations of linear viscoelastic polymer cantilever beams. *Comptes Rendus. Mécanique* 348 (10-11): 797-807.
<https://doi.org/10.5802/crmeca.15>.
- Doube, M., Kłosowski, M. M., Arganda-Carreras, I., Cordelières, F., Dougherty, R., Jackson, J. S., Schmid, B., Hutchinson, J. R., & Shefelbine, S. J. (2010). BoneJ: Free and extensible bone image analysis in ImageJ. *Bone*, 47(6), 1076–1079.
<https://doi.org/10.1016/j.bone.2010.08.023>
- Flores, N., Rao, G., Berton, E., & Delattre, N. (2019). The stiff plate location into the shoe influences the running biomechanics. *Sports Biomechanics*, 1–16.
<https://doi.org/10.1080/14763141.2019.1607541>
- Franz, J. R., Wierzbinski, C. M., & Kram, R. (2012). Metabolic cost of running barefoot versus shod: Is lighter better? *Medicine and Science in Sports and Exercise*, 44(8), 1519–1525. <https://doi.org/10.1249/MSS.0b013e3182514a88>
- Frederick, E. C. (1984). *Sport Shoes and Playing Surfaces*. Human Kinetics.

- Fuller, J. T., Bellenger, C. R., Thewlis, D., Tsiros, M. D., & Buckley, J. D. (2015). The effect of footwear on running performance and running economy in distance runners. *Sports Medicine (Auckland, N.Z.)*, 45(3), 411–422.
<https://doi.org/10.1007/s40279-014-0283-6>
- Gadot, B. (2015). Entangled single-wire NiTi material: A porous metal with tunable superelastic and shape memory properties. *Acta Materialia*, 13.
<https://doi.org/10.1016/j.actamat.2015.06.018>
- Gibson, I. J., & Ashby, M. F. (1982). The mechanics of three-dimensional cellular materials. *Proceedings of the Royal Society of London. A. Mathematical and Physical Sciences*, 382(1782), 43–59. <https://doi.org/10.1098/rspa.1982.0088>
- Gibson, L. J., & Ashby, M. F. (1999). *Cellular Solids: Structure and Properties*. Cambridge University Press. <https://doi.org/10.1017/CBO9781139878326>
- Guiraud, O., Dumont, P.J.J., Orgéas, L., Favier, D. (2012) . Rheometry of compression moulded fibre-reinforced polymer composites: rheology, compressibility, and friction forces with mould surfaces. *Composites Part A: Applied Science and Manufacturing*. <https://doi.org/10.1016/j.compositesa.2012.06.006>
- Hoogkamer, W., Kipp, S., Spiering, B. A., & Kram, R. (2016). Altered Running Economy Directly Translates to Altered Distance-Running Performance. *Medicine and Science in Sports and Exercise*, 48(11), 2175–2180.
<https://doi.org/10.1249/MSS.0000000000001012>
- Kinoshita, H., & Bates, B. T. (1996). The effect of environmental temperature on the properties of running shoes. *Journal of Applied Biomechanics*, 12(2), 258–268.
<https://doi.org/10.1123/jab.12.2.258>
- Le Cam, J.-B., Huneau, B., & Verron, E. (2008). Description of fatigue damage in carbon black filled natural rubber. *Fatigue & Fracture of Engineering Materials*

- & *Structures*, 31(12), 1031–1038. <https://doi.org/10.1111/j.1460-2695.2008.01293.x>
- Li, T.-T., Wang, H., Huang, S.-Y., Lou, C.-W., & Lin, J.-H. (2019). Bioinspired foam composites resembling pomelo peel: Structural design and compressive, bursting and cushioning properties. *Composites Part B: Engineering*, 172, 290–298. <https://doi.org/10.1016/j.compositesb.2019.04.046>
- Lippa, N., Hall, E., Piland, S., Gould, T., & Rawlins, J. (2014). Mechanical Ageing Protocol Selection Affects Macroscopic Performance and Molecular Level Properties of Ethylene Vinyl Acetate (EVA) Running Shoe Midsole Foam. *Procedia Engineering*, 72, 285–291. <https://doi.org/10.1016/j.proeng.2014.06.082>
- Madden, R., Sakaguchi, M., Tomaras, E. K., Wannop, J. W., & Stefanyshyn, D. (2016). Forefoot bending stiffness, running economy and kinematics during overground running. *Footwear Science*, 8(2), 91–98. <https://doi.org/10.1080/19424280.2015.1130754>
- Malisoux, L., Delattre, N., Urhausen, A., & Theisen, D. (2019). Shoe cushioning, body mass and running biomechanics as risk factors for running injury: A study protocol for a randomised controlled trial. *Sports and Exercise Medicine*. <https://doi.org/10.1136/bmjopen-2017-017379>
- Mills, N. (2007). Running shoe case study, Chapter 13. In *Polymer Foams Handbook* (pp. 307–327). <https://doi.org/10.1016/B978-075068069-1/50014-3>
- Mullins, L. (1969). Softening of Rubber by Deformation. *Rubber Chemistry and Technology*, 42(1), 339–362. <https://doi.org/10.5254/1.3539210>
- Musgjerd, T., Anason, J., Rutherford, D., & Kernozek, T. W. (2021). Effect of Increasing Running Cadence on Peak Impact Force in an Outdoor Environment.

- International Journal of Sports Physical Therapy*, 16(4), 1076–1083.
<https://doi.org/10.26603/001c.25166>
- Mzabi, S., Berghezan, D., Roux, S., Hild, F., & Creton, C. (2011). A critical local energy release rate criterion for fatigue fracture of elastomers. *Journal of Polymer Science Part B: Polymer Physics*, 49(21), 1518–1524.
<https://doi.org/10.1002/polb.22338>
- Nigg, B. M. (Ed.). (1986). *Biomechanics of Running Shoes*. Human Kinetics.
- Nigg, B. M., Baltich, J., Maurer, C., & Federolf, P. (2012). Shoe midsole hardness, sex and age effects on lower extremity kinematics during running. *Journal of Biomechanics*, 45(9), 1692–1697.
<https://doi.org/10.1016/j.jbiomech.2012.03.027>
- Oeveren, B. T. van, Ruiter, C. J. de, Beek, P. J., & Dieën, J. H. van. (2017). Optimal stride frequencies in running at different speeds. *Plos One*, 12(10).
<https://doi.org/10.1371/journal.pone.0184273>
- Pardo-Alonso, S., Solórzano, E., Vicente, J., Brabant, L., Dierick, M. L., Manke, I., Hilger, A., Laguna, E., & Rodriguez-Perez, M. A. (2015). Micro-CT-Based Analysis of the Solid Phase in Foams: Cell Wall Corrugation and other Microscopic Features. *Microscopy and Microanalysis*, 21(5), 1361–1371.
<https://doi.org/10.1017/S1431927615014890>
- Patterson, B. M., Cordes, N. L., Henderson, K., Williams, J. J., Stannard, T., Singh, S. S., Ovejero, A. R., Xiao, X., Robinson, M., & Chawla, N. (2016). In situ X-ray synchrotron tomographic imaging during the compression of hyper-elastic polymeric materials. *Journal of Materials Science*, 51(1), 171–187.
<https://doi.org/10.1007/s10853-015-9355-8>

- Schindelin, J., Arganda-Carreras, I., Frise, E., Kaynig, V., Longair, M., Pietzsch, T., Preibisch, S., Rueden, C., Saalfeld, S., Schmid, B., Tinevez, J.-Y., White, D. J., Hartenstein, V., Eliceiri, K., Tomancak, P., & Cardona, A. (2012). Fiji: An open-source platform for biological-image analysis. *Nature Methods*, 9(7), 676–682. <https://doi.org/10.1038/nmeth.2019>
- Shen, Y., Golnaraghi, F., & Plumtree, A. (2001). Modelling compressive cyclic stress strain behaviour of structural foam. *International Journal of Fatigue*, 23(6), 491–497. [https://doi.org/10.1016/S0142-1123\(01\)00014-7](https://doi.org/10.1016/S0142-1123(01)00014-7)
- Shimazaki, Y., Nozu, S., & Inoue, T. (2016). Shock-absorption properties of functionally graded EVA laminates for footwear design. *Polymer Testing*, 54, 98–103. <https://doi.org/10.1016/j.polymertesting.2016.04.024>
- Silva, R. M., Rodrigues, J. L., Pinto, V. V., Ferreira, M. J., Russo, R., & Pereira, C. M. (2009). Evaluation of shock absorption properties of rubber materials regarding footwear applications. *Polymer Testing*, 28(6), 642–647. <https://doi.org/10.1016/j.polymertesting.2009.05.007>
- Singaravelu, A. S. S., Williams, J. J., Ruppert, J., Henderson, M., Holmes, C., & Chawla, N. (2020). In situ X-ray microtomography of the compression behaviour of eTPU bead foams with a unique graded structure. *Journal of Materials Science*, 56(8), 5082–5099. <https://doi.org/10.1007/s10853-020-05621-3>
- Sun, X., Lam, W.-K., Zhang, X., Wang, J., & Fu, W. (2020). Systematic Review of the Role of Footwear Constructions in Running Biomechanics: Implications for Running-Related Injury and Performance. *Journal of Sports Science & Medicine*, 19(1), 20–37.

- Taunton, J. E., Ryan, M. B., Clement, D. B., McKenzie, D. C., Lloyd-Smith, D. R., & Zumbo, B. D. (2002). A retrospective case-control analysis of 2002 running injuries. *British Journal of Sports Medicine*, 36(2), 95–101.
<https://doi.org/10.1136/bjsm.36.2.95>
- Taylor, Samuel A., Peter D. Fabricant, M. Michael Khair, Amgad M. Haleem, et Mark C. Drakos. (2012). A Review of Synthetic Playing Surfaces, the Shoe-Surface Interface, and Lower Extremity Injuries in Athletes. *The Physician and Sportsmedicine* 40 (4): 66-72. <https://doi.org/10.3810/psm.2012.11.1989>.
- Taunton, J. E., Ryan, M., Clement, D., McKenzie, D., Lloyd-Smith, D., & Zumbo, B. (2003). A prospective study of running injuries: The Vancouver Sun Run ‘In Training’ clinics. *British Journal of Sports Medicine*, 37(3), 239–244.
<https://doi.org/10.1136/bjsm.37.3.239>
- Verdejo, Raquel. 2004. Gas Loss and Durability of EVA Foams Used in Running Shoes. PhD Thesis, UK: University of Birmingham.
<https://theses.bham.ac.uk/id/eprint/231/>.
- Verdejo, R., & Mills, N. J. (2002). Performance of EVA foam in running shoes. In *The Engineering of Sport* (Vol. 4, pp. 580–588). Blackwell Science.
- Verdejo, R., & Mills, N. J. (2004a). Heel–shoe interactions and the durability of EVA foam running-shoe midsoles. *Journal of Biomechanics*, 37(9), 1379–1386.
<https://doi.org/10.1016/j.jbiomech.2003.12.022>
- Verdejo, R., & Mills, N. J. (2004b). Simulating the effects of long distance running on shoe midsole foam. *Polymer Testing*, 23(5), 567–574.
<https://doi.org/10.1016/j.polymertesting.2003.11.005>

Zhang, D., Scarpa, F., Ma, Y., Boba, K., Hong, J., & Lu, H. (2013). Compression mechanics of nickel-based superalloy metal rubber. *Materials Science and Engineering: A*, 580, 305–312. <https://doi.org/10.1016/j.msea.2013.05.064>

Appendices

Parameters for the X-ray tomography at macroscale

At macroscale, *i.e.*, to visualize the vertical slices of soles shown in Fig. 1b, we use a laboratory X-ray tomograph from RX Solutions with the following parameters: source type: Hamamatsu equipped with a tungsten filament, mode: large spot, detector flat panel: VARIAN, tension: 150 kV, target current: 450 μA , frame rate: 12 s^{-1} , number of averaged frames: 6, number of projections: 2240, so as to obtain a $100^3 \mu\text{m}^3$ voxel size.

Image analysis

A 3D region of interest (ROI) was defined in the core of each reconstructed volume as a representative volume element for which the following structural properties converge to constant values (Benedetti et al., 2021) and that avoid any edge effects due to image acquisition or to sample preparation (dimensions: $750 \times 750 \times 750 \mu\text{m}^3$).

The different phases of the sample were segmented for descriptor quantification, and to refine this step, the plugin Trainable Weka Segmentation 3D (Arganda-Carreras et al., 2017) was used together with a Fast Random Forest algorithm to keep very thin cellular walls. A zoom in the ROI is presented in Fig. SIa where the white, the green and the red colours represent respectively the mineral fillers, the elastomeric walls and the cells. The classifier was trained by the operator using the mean and the variance of grey level of neighbour voxels to segment phases, as shown in Fig. SIb and c in the 2D and 3D black

and white renderings. Porosity ϕ , was obtained by dividing the number of pore voxels by the total number of voxels in the ROI. The wall thickness, t , was evaluated using the *Thickness* function of the plugin BoneJ (Doubé et al., 2010) in which for each voxel of the solid phase, the greatest sphere diameter, that fits within the structure and contains the voxel, is given. The cell size, C , was evaluated using this same function on the cell to give a representative diameter of the largest sphere contained in cells, knowing that for anisotropic cells, the value under-estimated their real size.

Tables

Table1. Foams under study and their properties.

Foam	Polymer	Lightness	Cushioning	Rebound	Durability
F ₁	EVA		X	X	X
F ₂ , F ₂ *	EVA	X	X		X
F ₃	TPU		X		X
F ₄	PEBA	X		X	

Table 2. Structural descriptors and mechanical properties during N=1.

		F ₁	F ₂	F ₂ *	F ₃	F ₄
S t r u c t u r a l	ρ (g cm ⁻³)	0.17 ± 0.02	0.13 ± 0.02	0.23 ± 0.02	0.24 ± 0.02	0.09 ± 0.02
	ϕ (-)	0.79 ± 0.02	0.79 ± 0.02	0.71 ± 0.02	0.72 ± 0.02	0.90 ± 0.02
	C (μm)	80 ± 47 %	35 ± 29 %	111 ± 46 %	-	87 ± 36 %
	t (μm)	19 ± 44 %	5 ± 23 %	33 ± 61 %	-	10 ± 19 %
M e c h a n i c a l	σ_c (MPa)	0.1 ± 0.1	0.1 ± 0.1	0.1 ± 0.1	0.1 ± 0.1	-
	σ_{max}/ρ (MPa cm ³ g ⁻¹)	7.2 ± 0.2	8.8 ± 0.2	3.9 ± 0.2	3.3 ± 0.3	6.4 ± 0.1
	W_{abs}^{max}/ρ (mJ g ⁻¹)	3.9 ± 0.1	4.9 ± 0.1	2.7 ± 0.1	2.1 ± 0.1	3.6 ± 0.1
	η (-)	0.13 ± 0.01	0.14 ± 0.01	0.12 ± 0.01	0.05 ± 0.01	0.06 ± 0.01
	ε^{res} (-)	0.16 ± 0.02	0.15 ± 0.01	0.14 ± 0.01	0.05 ± 0.02	0.09 ± 0.01

Figures

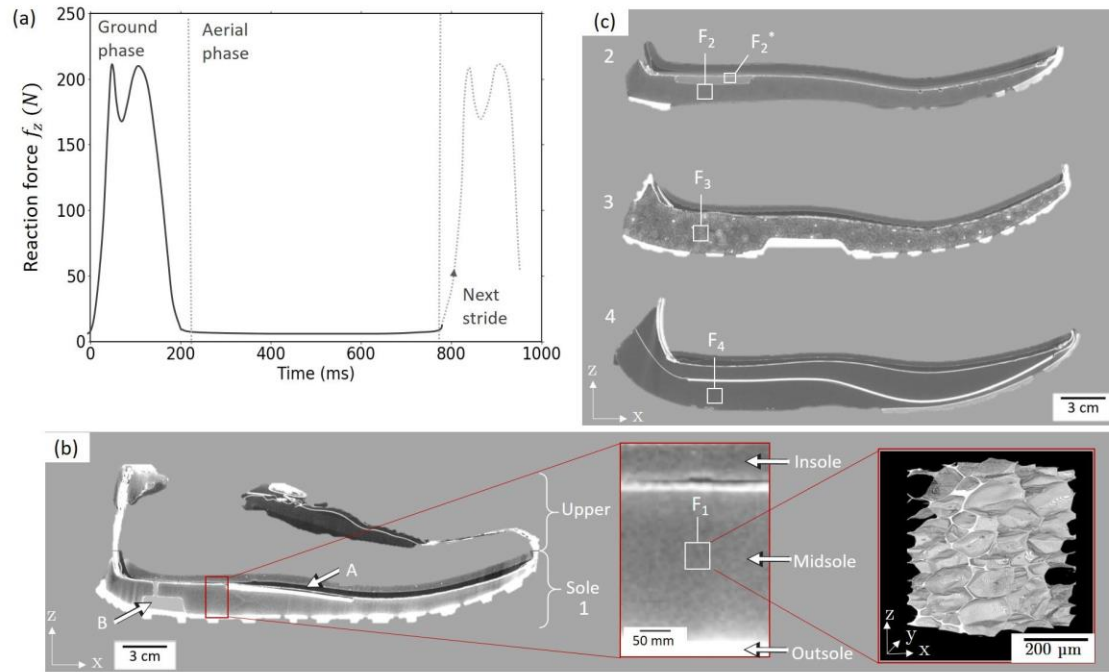


Figure 1. (a) Reaction foot-ground force f_z during a stride of a runner (75 kg, 12 km h⁻¹), adapted from previous studies (Clarke et al., 1983; Nigg, 1986). (b) Vertical slice obtained by X-ray tomography of the first studied running shoe with a zoom on the sole structure and on the 3D microstructure of its midsole foam F_1 obtained by X-ray microtomography. (A) Stiffer plate and (B) air volume inserted in the midsole. (c) Vertical slices obtained by X-ray tomography of the other studied soles and their respective midsoles F_2 , F_2^* , F_3 and F_4 (for (b) and (c), see materials and methods for acquisition parameters and shoes information).

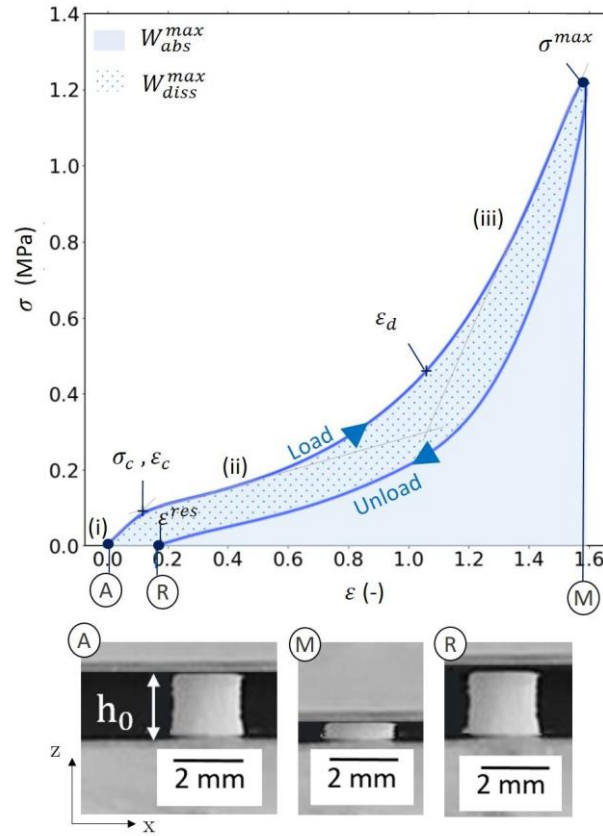


Figure 2. Typical stress-strain behaviour (case of foam F1) during the first compression cycle. The three densification phases during loading are noted (i), (ii) and (iii). (A) illustration of a typical undeformed sample (case of foam F1) mounted between the compression platens, corresponding to ε^0 , (M) same sample at maximum strain ε^{max} and (R) at residual strain ε^{res} .

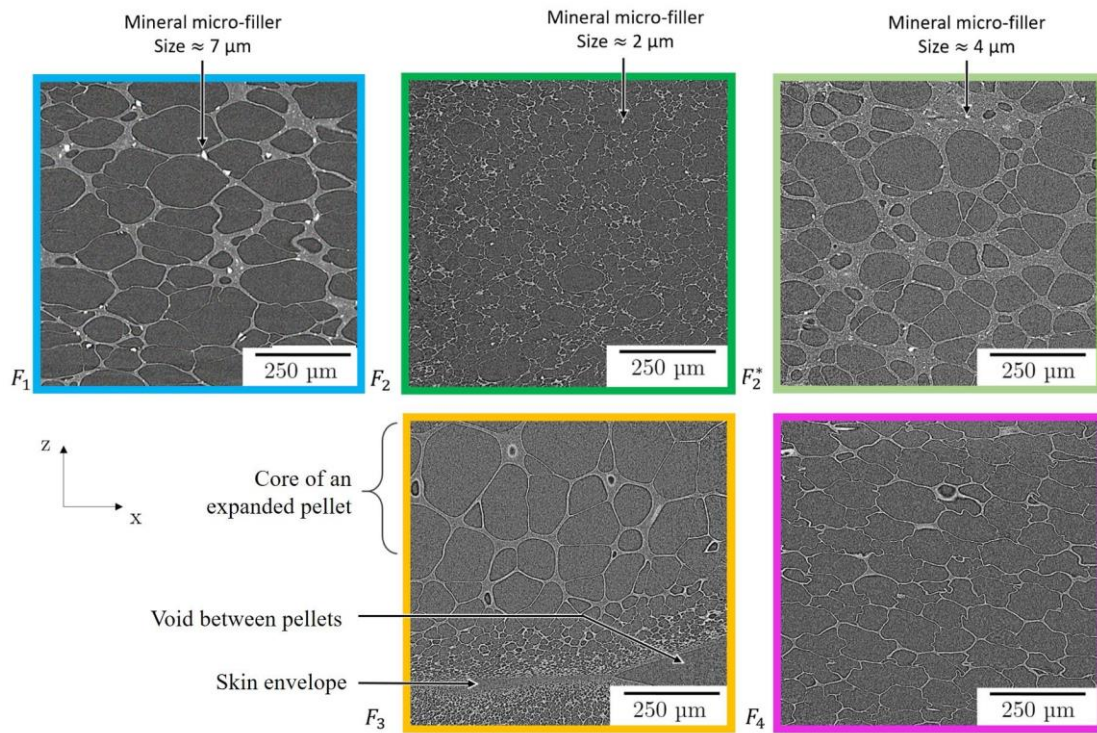


Figure 3. 2D grey levels slices obtained by μCT showing the inner microstructure the studied foams along the compression plane.

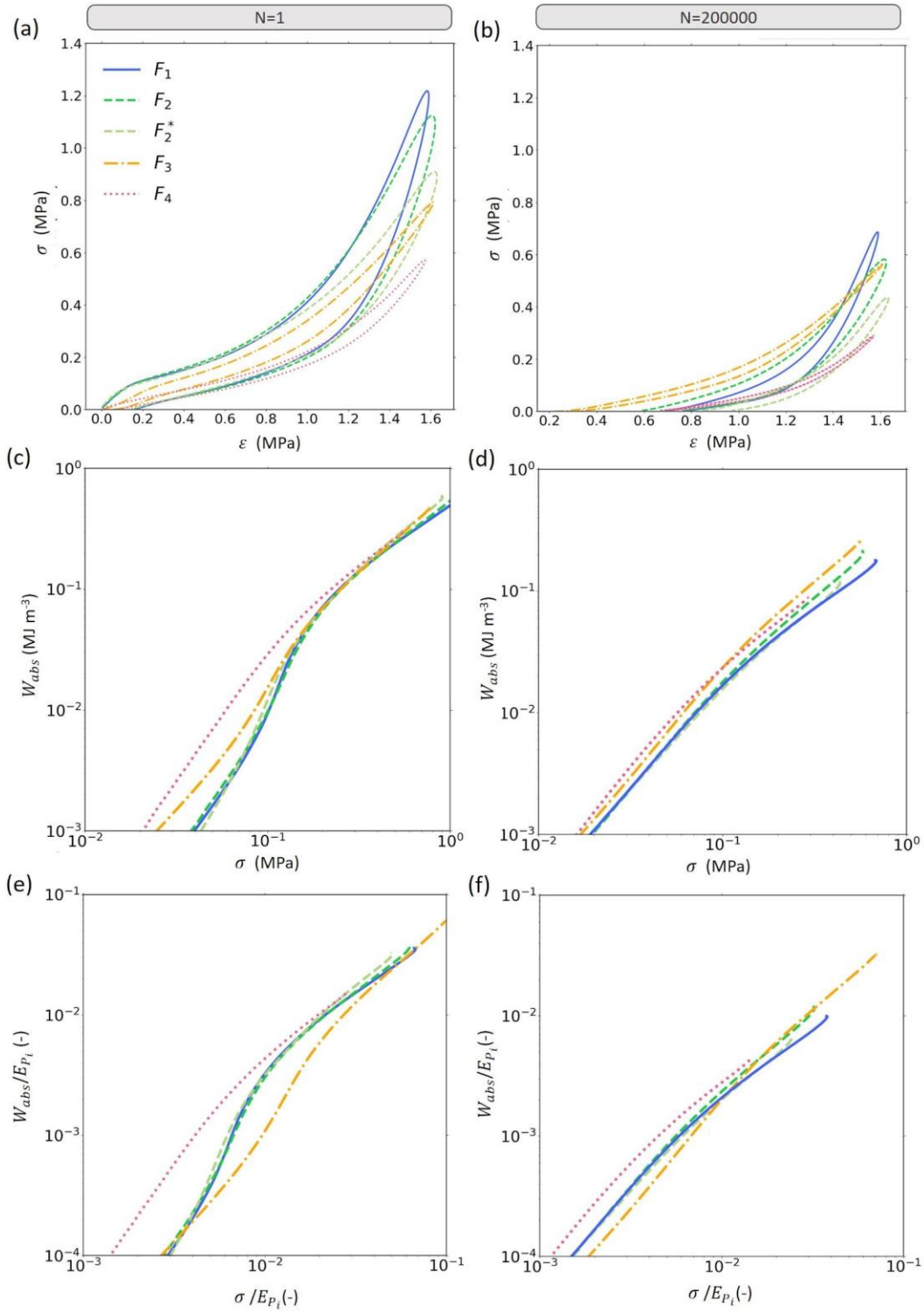


Figure 4. Stress-strain behaviour of all foams at (a) $N = 1$ and (b) $N = 200000$. Volumetric absorbed energy diagram at (c) $N = 1$ and (d) $N = 200000$. Volumetric absorbed energy diagram normalized by the Young modulus of the foam parent polymer at (e) $N = 1$ and (f) $N = 200000$.

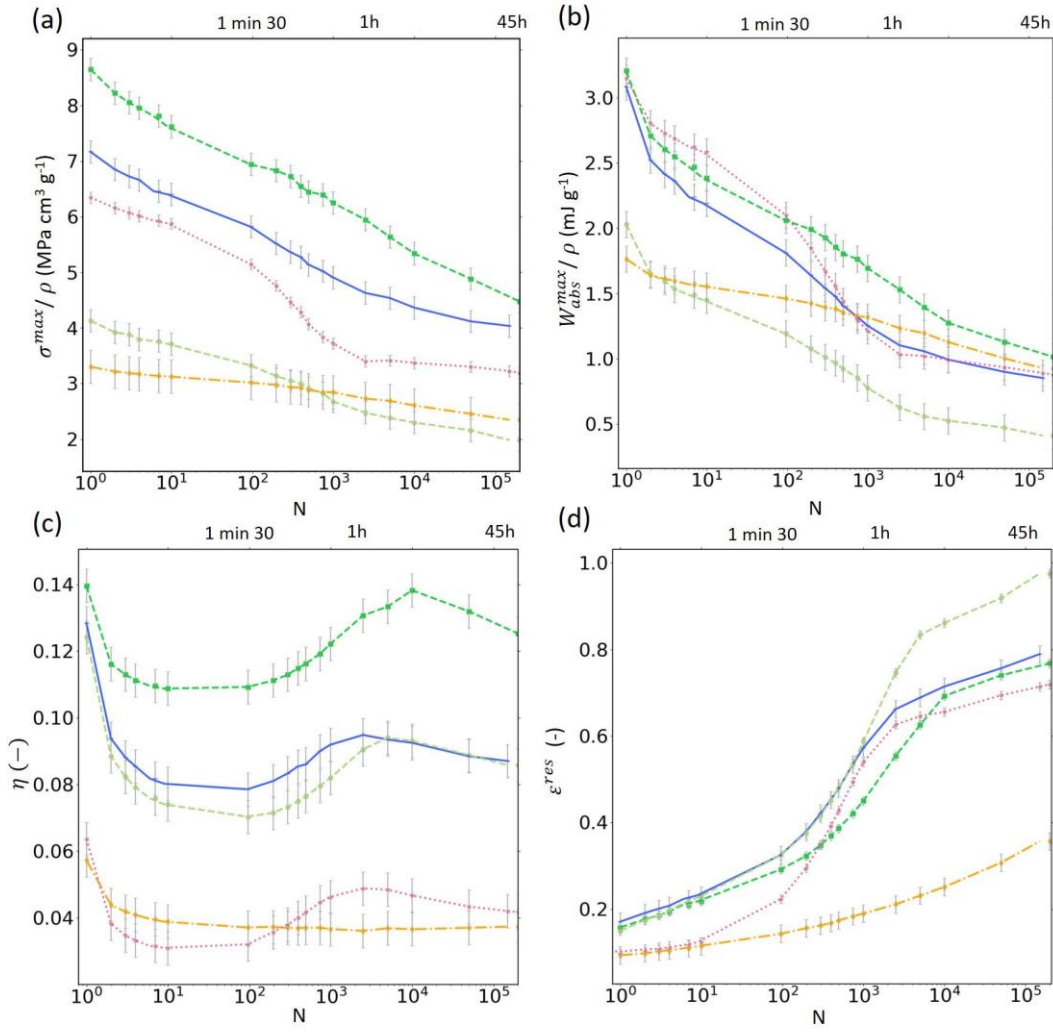


Figure 5. Evolution of (a) the maximum specific stress, (b) the maximum specific volumetric absorbed energy, (c) the damping loss factor and (d) the residual strain, as a function of the number of compression cycles for all foams. The errors bars represent the standard deviation of the data of the three tested sample. The legend is the same as Fig. 4.

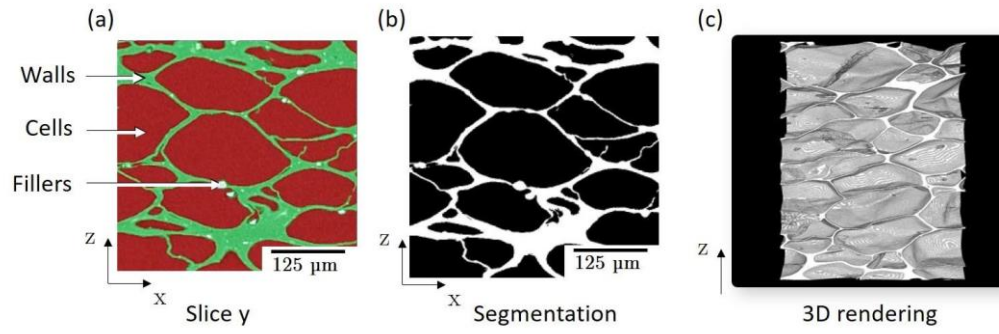


Figure SI. Zooms in the ROI of the foam F_1 showing (a) the fillers in white, the elastomeric walls in green and the cells in red, (b) the solid-gas phases segmentation obtained in 2D and (c) in 3D.

Figure captions

Figure 1. (a) Reaction foot-ground force f_z during a stride of a runner (75 kg, 12 km h⁻¹), adapted from previous studies (Clarke et al., 1983; Nigg, 1986). (b) Vertical slice obtained by X-ray tomography of the first studied running shoe with a zoom on the sole structure and on the 3D microstructure of its midsole foam F₁ obtained by X-ray microtomography. (A) Stiffer plate and (B) air volume inserted in the midsole. (c) Vertical slices obtained by X-ray tomography of the other studied soles and their respective midsoles F₂, F₂*, F₃ and F₄ (for (b) and (c), see materials and methods for acquisition parameters and shoes information).

Figure 2. Typical stress-strain behaviour (case of foam F₁) during the first compression cycle. The three densification phases during loading are noted (i), (ii) and (iii). (A) illustration of a typical undeformed sample (case of foam F₁) mounted between the compression platens, corresponding to ε^0 , (M) same sample at maximum strain ε^{max} and (R) at residual strain ε^{res} .

Figure 3. 2D grey levels slices obtained by μ CT showing the inner microstructure the studied foams along the compression plane.

Figure 4. Stress-strain behaviour of all foams at (a) $N = 1$ and (b) $N = 200000$. Volumetric absorbed energy diagram at (c) $N = 1$ and (d) $N = 200000$. Volumetric absorbed energy diagram normalized by the Young modulus of the foam parent polymer at (e) $N = 1$ and (f) $N = 200000$.

Figure 5. Evolution of (a) the maximum specific stress, (b) the maximum specific volumetric absorbed energy, (c) the damping loss factor and (d) the residual strain, as a function of the number of compression cycles for all foams. The errors bars represent the standard deviation of the data of the three tested sample. The legend is the same as Fig. 4.

Figure SI. Zooms in the ROI of the foam F_1 showing (a) the fillers in white, the elastomeric walls in green and the cells in red, (b) the solid-gas phases segmentation obtained in 2D and (c) in 3D.